

# Tuning Epitaxial Growth of Nb on MgO(100)

Laura Guasco,\* Liz Montañez Huaman, Yury N. Khaydukov, Thomas Keller, and Sabine Pütter\*

**Abstract:** Niobium thin films are central to many applications, such as superconducting radio-frequency cavities and superconducting qubits, due to its relatively high superconducting temperature and easiness to form heterostructures. However, literature on epitaxial growth of Nb on one of the most commonly used substrates, that is MgO, reports contradicting results. In the present parametric study, a coherent picture of how the crystalline orientation and the film morphology depend on the growth parameters is presented. The effects of growth parameters such as growth temperature, growth rate, deposition technique, and surface quality on the transport properties of the superconductor are discussed. In light of the new findings, an overview on previously published results and proposed nucleation and growth mechanisms is also given.

## 1. Introduction

Thin Nb layers are crucial for research and applications in various fields. Niobium is a superconductor with the highest superconducting transition temperature among elemental metals ( $T_C=9.3$  K in bulk). In this respect two main applications are the superconducting radio-frequency cavities for particle accelerators,<sup>[1]</sup> and Josephson junctions,<sup>[2,3]</sup> which are the basis of superconducting qubit operation.<sup>[4]</sup> In addition, niobium is able to form high-quality interfaces with various non-superconducting materials, which makes Nb-based heterostructures promising in many applications of superconducting electronics.<sup>[5]</sup> In many cases a

high purity and crystalline quality of niobium film is required to achieve the desired functionality.<sup>[6–8]</sup> Niobium is also known to be a strong hydrogen absorber with a rich phase diagram depending on temperature, pressure, film thickness, and structural quality.<sup>[9–13]</sup> Epitaxial Nb films are often used as a buffer layer for controllable growth of rare-earth films,<sup>[14,15]</sup> exchange biased,<sup>[16]</sup> and GMR systems.<sup>[17]</sup> Thus, the controlled growth of niobium films with a given crystal orientation and high quality of the layer and surface is an important task for many areas of science and technology.

Driven by these strong motivations, the issue of controlled growth of niobium

epitaxial films has been studied for several decades. A collection of numerous studies of the deposition of niobium on a sapphire substrate can be found in the review of Wildes et al.<sup>[18]</sup> In particular, it was shown that niobium epitaxial films can be grown on sapphire at an elevated substrate temperature (750–900 °C). Moreover, the crystalline direction of film growth can be specified by choosing a proper orientation of the sapphire substrate. For example, Nb(110) films grow on Al<sub>2</sub>O<sub>3</sub>(1120) substrates, while Al<sub>2</sub>O<sub>3</sub>(1102) orientation leads to Nb(100) growth.


The situation is different for Nb growth on MgO(001) which is investigated in this publication. Bulk niobium exhibits a bcc crystal structure with cell parameter  $a_{\text{Nb}} = 3.32$  Å while the lattice parameter of MgO is  $a_{\text{MgO}} = 4.21$  Å. It is known from literature that there are two possible growth orientations, that is, Nb(100) and Nb(110) on MgO(100).<sup>[19]</sup> For Nb(100) the preferred orientation due to lower lattice mismatch is Nb(100)[011]||MgO(100)[001], with a lattice constant ratio  $a_{\text{MgO}}/(\sqrt{2}a_{\text{Nb}}) = 0.9$ . For Nb(110) two possible alignments exist: Nb(110)[011]||MgO(100)[001] and Nb(110)[011]||MgO(100)[010]. For the short lattice constant the length is the same for Nb(100) while for the other direction it is  $a_{\text{MgO}}/a_{\text{Nb}} = 1.3$ , see for example, refs. [20, 21].

Publications discussing how to obtain one or the other orientations are not complete and often contradictory. In a pioneering work, Hutchinson<sup>[19]</sup> reports: a) no dependence of Nb deposition rate within the used range (0.03–2 Å s<sup>−1</sup>) on structure; b) the epitaxial growth of thin (up to 25 nm) Nb films in (100) orientation at temperatures 500–600 °C; and c) the emergence of regions of Nb(110) for thicker films. In a more recent work, Beringer et al. discuss in a combined study of varied growth rate and surface quality that both parameters influence the crystallographic orientation.<sup>[20]</sup> On an in situ annealed MgO(100) substrate Nb grew in (110) orientation for the growth rate of 0.32 Å s<sup>−1</sup>, while at a rate of 0.48 Å s<sup>−1</sup> on a substrate with MgO seed layer the (100)

L. Guasco, Y. N. Khaydukov, T. Keller  
Max-Planck-Institut für Festkörperforschung  
Heisenbergstraße 1, D-70569 Stuttgart, Germany  
E-mail: L.Guasco@fkf.mpg.de

L. Guasco, Y. N. Khaydukov, T. Keller  
Max Planck Society Outstation at the Heinz Maier-Leibnitz Zentrum (MLZ)  
D-85748 Garching, Germany

L. M. Huaman, S. Pütter  
Forschungszentrum Jülich GmbH  
Jülich Centre for Neutron Science (JCNS) at Heinz Maier-Leibnitz Zentrum (MLZ)  
Lichtenbergstr. 1, D-85747 Garching, Germany  
E-mail: s.puetter@fz-juelich.de

 The ORCID identification number(s) for the author(s) of this article can be found under <https://doi.org/10.1002/apxr.202200122>

© 2023 The Authors. Advanced Physics Research published by Wiley-VCH GmbH. This is an open access article under the terms of the Creative Commons Attribution License, which permits use, distribution and reproduction in any medium, provided the original work is properly cited.

DOI: 10.1002/apxr.202200122

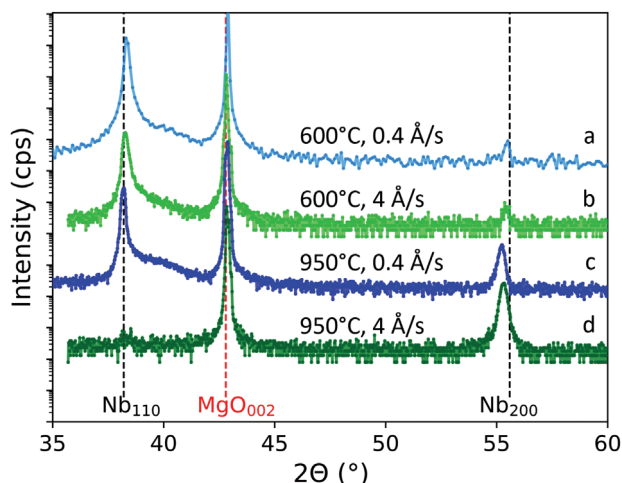


**Figure 1.** Comparison of XRD patterns of Nb films grown either at 600 °C or at 950 °C with varying growth rate (low rate: 0.4 Å s<sup>-1</sup>, high rate: 4 Å s<sup>-1</sup>). Please note the logarithmic scale of the y-coordinate.

orientation was observed for films of 10 to 1000 nm thickness grown at 600 °C. In contrast to Hutchinson<sup>[19]</sup> no appearance of (110) orientation for thick films was reported. Fu et al. grew 180 nm Nb on MgO(100) at 950 °C and 5 Å s<sup>-1</sup> and report Nb(100).<sup>[22]</sup>

The intention of this work is to disentangle the effect of various deposition parameters on the structural and transport properties of niobium films in a more systematic way utilizing in situ reflection high energy electron diffraction (RHEED) and ex situ X-ray diffraction (XRD), atomic force microscopy (AFM), and transport measurements. Our results not only help to explain several seemingly discording previous works, but as well offer a comprehensive overview on the complex growth of Nb films on MgO.

## 2. Results and Analysis

### 2.1. Influence of Varying Growth Rate

**Figure 1** shows the XRD measurements on Nb thin film samples grown at 600 °C and 950 °C in combination with the growth rates of 0.4 and 4 Å s<sup>-1</sup>. The temperatures and growth rates were chosen with respect to the above mentioned published results. To protect the Nb surface against oxidation, all samples are covered by 3 nm Pt. Obviously, sample d confirms the Nb(100) orientation observed by Fu et al. and sample a agrees with the findings of Beringer et al. as there is a dominant Nb(110) peak. Hence, both results are reproduced. Nb(110) is also observed at high growth rate at 600 °C (sample b). The presence of the faint (200) peak of samples a and b will be discussed in Section 2.3. Reducing the growth rate at 950 °C leads to prevalent Nb(110) growth (sample c).

The results are reflected in AFM and RHEED measurements, **Figure 2**. The RHEED patterns (**Figure 2a,b**) look the same at 600 °C independent of the growth rate, with two sets of surface streaks, that correspond to the two possible alignments of the Nb(110) elementary cell. Both high temperature RHEED patterns reveal chevrons which are correlated with faceting. At high growth rate the RHEED pattern rather resembles a transmission pattern (**Figure 2d**) while for low growth rate (**Figure 2c**) we ob-

serve a more complex pattern, which will be discussed in the following section.

The bottom of **Figure 2** shows ex situ AFM pictures taken after deposition. In spite of the Pt cover, the surface morphology of the Nb is expected to be reproduced, as Pt is known to grow layer-by-layer on Nb(110) single crystals at room temperature (RT).<sup>[23]</sup> Moreover, the measured height variation is more than 6 nm and consequently higher than the Pt layer thickness. The AFM images of the Nb films grown at 600 °C confirm once again the minor influence of the growth rate on the surface morphology, see **Figure 2e,f**. A biaxial morphology is observed in both images, only the structure size is different. This biaxial morphology observed in real space is consistent with the two in-plane alignments found by RHEED. Similar surface structure was found by Beringer et al. for non-covered Nb(110) surface.<sup>[20]</sup> In contrast, at 950 °C there are flat, large islands with straight edges for low growth rate (**Figure 2g**) which change to smaller structures with frayed edges at high growth rate (**Figure 2h**).

It should be noted that the thickness of the high growth rate samples is 50 nm while it is 100 nm for all other. As only the bulk structure is compared, this will not have a relevant impact on the final assessment of the results.

To summarize, Nb(110) is achieved at 600 °C independent of the growth rate while at 950 °C the high growth rate enables Nb(100) growth. As for MBE growth the low growth rate is quite common, we now proceed to examine the effect of the growth temperature.

### 2.2. Variation of the Growth Temperature

**Figure 3** shows XRD measurements of 100 nm Nb thin films grown at different substrate temperature at low growth rate of 0.4 Å s<sup>-1</sup>. Up to the growth temperature of 600 °C a strong Nb(110) peak is visible, with relaxation to the bulk lattice constant with increasing temperature. Above 600 °C the Nb(200) peak becomes dominant, in combination with a weaker Nb(110) peak. At 950 °C the Nb(110) peak is dominant again while the Nb(200) peak is small.

Analysis of 2D scattering maps of the XRD measurements reveals textured epitaxial growth of the Nb layers at all temperatures. Examples are given in **Figure S1b–e**, Supporting Information. Rocking scans taken at the maximum of the main Bragg peak show a broadening for lower growth temperature. This is quantified by considering the full width half maximum (FWHM) of the peaks (see **Figure 4a**). The value gives the mean spread in orientation of the different out-of-plane crystalline domains of a perfect crystal with mis-orientation. The FWHM of the (110) peak decays with increasing temperature, while the (200) peak, dominant between 650 °C and 900 °C is rather constant. The corresponding rocking scans are given in **Figure S2**, Supporting Information. At 950 °C the FWHM is about 0.21°. Du et al. report for Nb(110)/Al<sub>2</sub>O<sub>3</sub>(1120) a larger FWHM of 0.385°. <sup>[24]</sup> Hence, one may say that the mosaicity of Nb(110) thin films grown at 600 °C and 950 °C on MgO(001) is comparable, if not better than that observed on sapphire substrates.

Of main interest for applications are the transport properties. The residual resistivity ratio (RRR), which is an indication of the amount of defects, and the critical temperature for

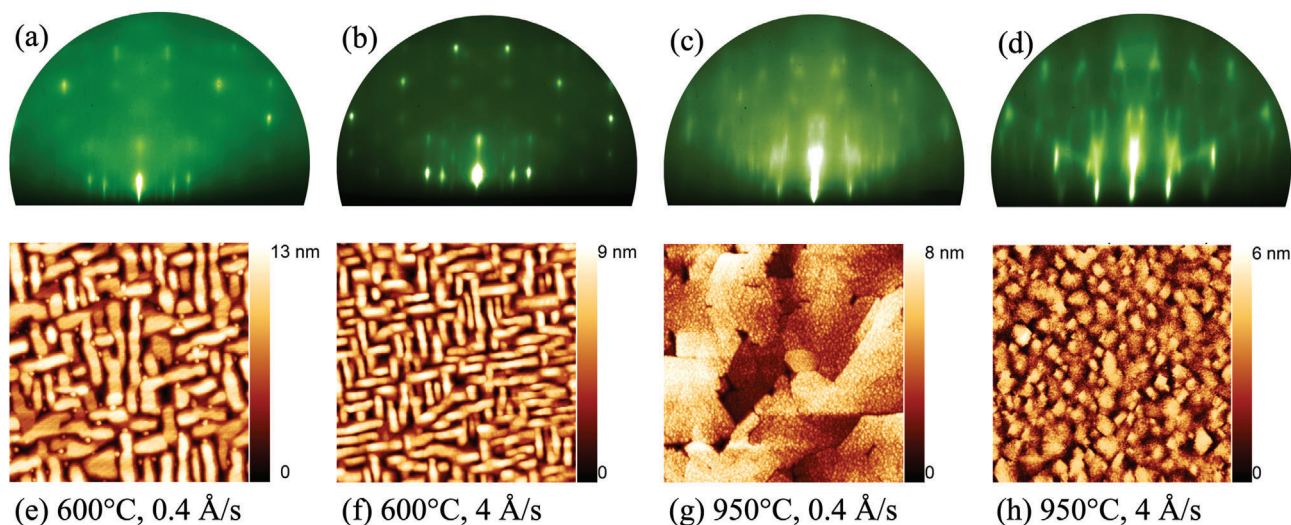


**Figure 2.** RHEED patterns (top row) and AFM images (bottom row) of Nb thin films grown at 600 °C (a,b,e,f) and at 950 °C (c,d,g,h) with rates 0.4 (a,e,c,g) and 4 Å s<sup>-1</sup> (b,f,d,h) as indicated in the bottom of each column. For RHEED, the e-beam orientation was parallel to MgO[100]. The AFM images were taken after deposition of a 3 nm Pt cap layer. The scan size is 1 μm × 1 μm.

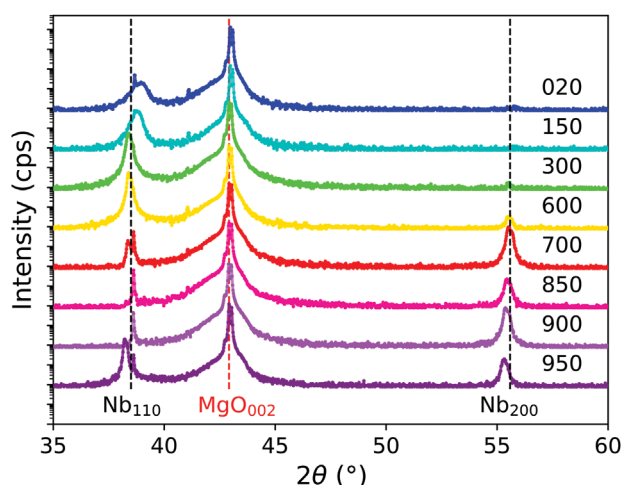


**Figure 3.** XRD measurements of Nb samples grown on MgO(001) at different temperatures (indicated on the right in °C) and growth rate of 0.4 Å s<sup>-1</sup> with nominal thickness of 100 nm. The dashed lines are guides to the eye following the bulk value of the Bragg peaks. Please note the logarithmic scale of the y-coordinate.

superconductivity  $T_C$  were measured. Figure 4b shows a slight but steady increase of RRR up to 600 °C, followed by a strong increase up to 700 °C and a sudden drop afterward. The maximum RRR of 60 is one of the highest values observed for Nb film of similar Nb thickness.<sup>[7,25]</sup>  $T_C$  increases slowly and drops significantly down above 700 °C, as shown in Figure 4c. These results seem to be unrelated to the dominant crystalline orientation, contrarily the observations of Krishnan et al.,<sup>[26]</sup> but are more correlated to the different grain morphology, as we will show in the following sections.

Hence, four different growth regimes can be distinguished: in the low temperature growth up to 600 °C (region I) there is Nb(110) growth, above 600 °C up to 700 °C (region II) there is

a transition with high RRR and Nb(100) orientation, then from 750 °C up to 900 °C still Nb(100) exists (region III), albeit with strongly reduced RRR, and finally above 950 °C there is again dominant Nb(110) growth (region IV).

Also, the RHEED patterns corroborate the presence of four different growth regimes, see Figure 5. In the top row images the e-beam is oriented parallel to MgO[100] while it is parallel to MgO[110] for the bottom row images. For room temperature growth up to 600 °C the RHEED pattern of Nb reveals two sets of surface streaks of zeroth order (e-beam parallel to MgO[100]), see Figures 2a and 5a. The ratios of the distances between the reflections of Nb and MgO(100) are 0.9 and 1.3, in agreement with the two lattice orientations (domains) expected for (110) growth of Nb.<sup>[20]</sup> With e-beam in MgO[110] direction (Figure 5e) there is an equal contribution of both (110) domains, which gives an average ratio of the lattice constants of about 1.1.

The transition growth region (above 600 °C up to 700 °C) is characterized by a Nb(100) crystalline structure, see Figure 3. In both e-beam directions the RHEED patterns are characterized by a mixture of spots, which can be ascribed to the (100) orientation, and Debye–Scherrer rings, which identify polycrystalline growth, Figure 5b,f. Please note that these rings appear only upon the cooling of films to room temperature, indicating a surface reconstruction process.

Above 700 °C a clear crystalline structure of Nb(100) is visible in the RHEED patterns, Figure 5c,g. In addition, there are chevrons, which indicate faceting (Figure 5c). The investigation of the zeroth order of the reflexes gives a ratio of 0.9, as in the previous region, consistent with (100) orientation. In MgO[110] direction a 2-d surface RHEED pattern is visible with a superstructure. The details of the origin of this pattern are not further pursued. At 950 °C the RHEED patterns are difficult to interpret. However, taking a closer look a superposition of the patterns of region I (dominant) and region III is observed. This is in line with the XRD results which reveal at this temperature both, Nb(110) and Nb(100) peaks.



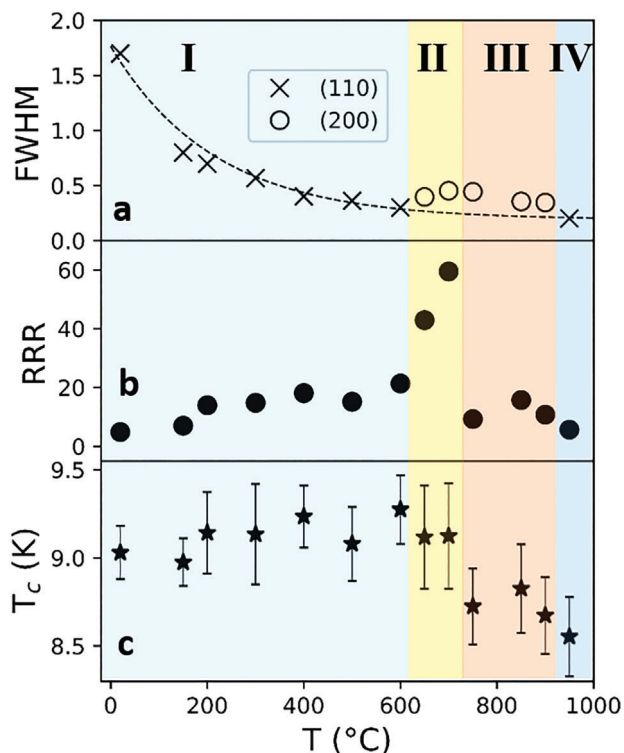


**Figure 4.** Summary of crystallographic and transport properties of Nb films versus deposition temperature. The colored background represents different growth regimes. Panel a shows FWHM of the rocking scan of the dominant Bragg peaks. The dashed line is a guide to the eye. Panels b and c show the RRR and superconducting transition temperature  $T_c$ . The  $\Delta T_c$  is shown as errorbar in c.

The surface morphology of Pt/Nb/MgO(001) grown at different temperatures was also investigated with AFM, see **Figure 6**. In the low temperature regime the biaxial morphology discussed in the previous section is observed, see Figures 2e and 6a. In addition, there is an increase in grain size from 45 to 70 nm with increasing Nb growth temperature. The surface structure changes above 650 °C, in the transition growth regime II. Here, the surface is covered by spherical islands of about 50–80 nm in diameter. The root mean square (RMS) roughness is about 1 nm. Above 750 °C the surface becomes fractured. The grain size increases to 100 nm and the surface roughness decreases to 0.3 nm. We notice that both, AFM images and RHEED patterns in regime III are similar to those obtained for Nb(100) at high growth rate and at 950 °C, shown in Figure 6c. At 950 °C a platelet structure with a typical dimension of  $\approx 300$ –500 nm and low RMS surface roughness (0.8 nm) is observed (Figure 6d).

Combining all observations we may state the following: In the low temperature regime, Nb grows in domains with (110) orientation, with biaxial grain morphology. At about 600 °C the crystalline growth changes from dominant (110) to (100) orientation. In this transition regime two regions are distinguished, one with homogeneous spherical grains (region II) and high RRR up to about 750 °C, and one with bigger fractured islands and low RRR above 750 °C (region III). At 950 °C Nb growth switches back to (110), forming large platelet structures with large facets.

### 2.3. Thickness Resolved Nb Growth

Utilizing in situ RHEED during deposition, Nb growth is investigated in dependence of thickness. **Figure 7** shows RHEED patterns of different growth stages of Nb at 500 °C with growth rate of  $0.4 \text{ \AA s}^{-1}$ . The e-beam was oriented parallel to the [100] direction of the MgO(100) substrate. The RHEED pattern of the annealed MgO substrate is characterized by sharp reflections and Kikuchi lines which indicate high surface quality, see Figure 7a. In the beginning of Nb growth, a reflection pattern with equidistant reflections appears while the substrate reflexes vanish (Figure 7b). The lattice spacing is the same as for the substrate, indicating epitaxial growth with the arrangement of Nb atoms following the MgO(100) structure underneath. At this early stage epitaxial Nb(100) growth on MgO(100) is observed at all growth temperatures.

Subsequent growth stages were measured with e-beam along MgO[100] to shed light on the differences between the crystalline orientations obtained in the various regions. For region I, at a critical thickness additional reflexes appear with the lattice distance of  $\sqrt{2} a_{\text{Nb}}$  which are related to Nb(110) growth, as shown in Figure 7c. This transformation thickness to Nb(110) growth decreases from about 23 Å at RT to about 13 Å at 600 °C. At 950 °C it is about the same, that is, 15 Å. For regime II the growth proceeds as follows: early stage (100) growth is quickly followed by (110) growth up to circa 4.5 nm, after which there is again (100) growth, which then persists until the end of the deposition. This mixture of different growth orientations is reflected in the XRD measurements (Figure 3) as well as in the RHEED patterns (Figure 5b,f). In regime III the situation is quite different, since after the early stage growth there are only reflections which can be attributed to (100) growth. In regime IV the pattern, though more blurred, seems to evolve similarly to that observed in regime I, Figure 5d.

Finally, all RHEED patterns measured after Pt deposition indicate crystalline growth, see example in Figure 7d.

## 3. Discussion

Contradicting results about Nb growth on MgO(100) were reported in the past as the growth of both crystalline orientations, that is, Nb(100) and Nb(110) on MgO(100), was observed. Indeed, the mechanisms which lead to growth of one or the other orientation were not fully understood. In the following, we focus on this open question.

At high growth temperature and high growth rate Fu et al.<sup>[22]</sup> observed Nb(100) growth on MgO(100) which is consistent with the present results. However, the authors' statement that Nb(100) was the only crystalline orientation to grow on single crystalline MgO(100) is rebutted. The reduction of the growth rate leads to prominent growth of Nb(110) at the same temperature and emphasizes that the growth mechanism is more complex. Obviously, both, growth rate and growth temperature play a significant role. We can try to shed some light on their role starting from the early stages of Nb growth on MgO(100).

Utilizing density functional theory (DFT) calculations, Shim and Amar studied the binding and adsorption energies for various types of mainly planar Nb clusters on MgO(100).<sup>[21]</sup> They

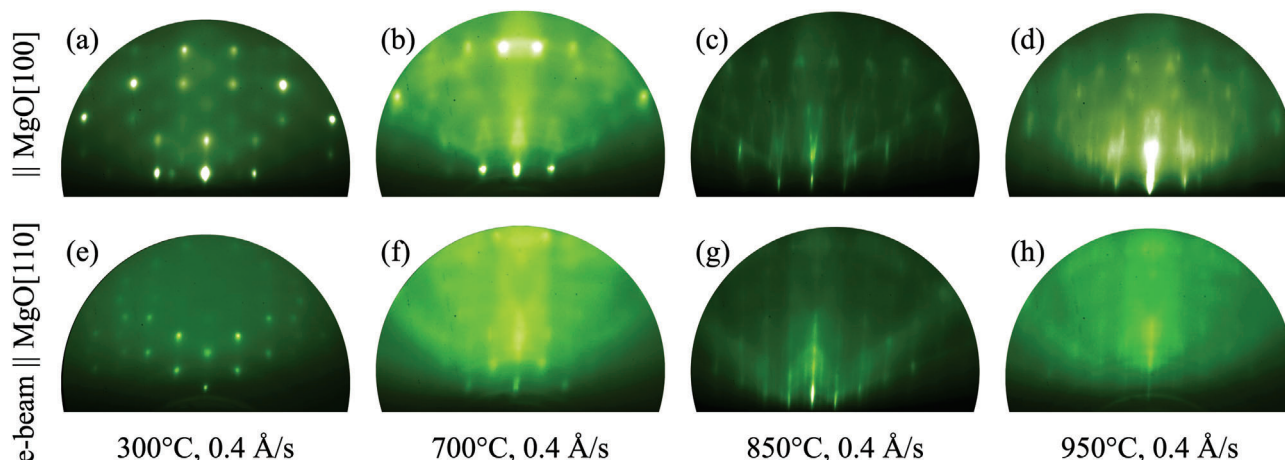


**Figure 5.** RHEED patterns after cooling down to RT for 100 nm Nb grown at 300 °C (a and e), at 700 °C (b and f), 850 °C (c and g) and at 950 °C (d and h). The e-beam orientation was parallel to MgO[100] for top row images and parallel to MgO[110] for bottom row images. The growth rate was always  $0.4 \text{ Å s}^{-1}$ .

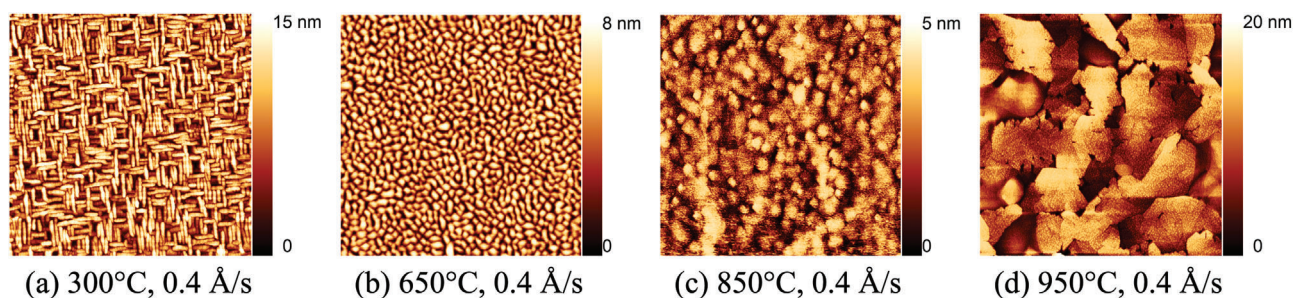


**Figure 6.** AFM scans of 3 nm Pt/100 nm Nb/MgO(001) with Nb deposited a) at 300 °C, b) at 650 °C, c) at 850 °C, and d) 950 °C. The scan size is  $2 \mu\text{m} \times 2 \mu\text{m}$ .

show that in absence of other point defects, the preferential adsorption takes place on the site of the oxygen atoms and that small Nb clusters prefer to grow in (100) orientation. However, for full monolayer coverage, the favored orientation is (110) which has, due to strain relaxation effects, higher binding energy of 5.46 eV in comparison to 4.96 eV for Nb(100).

These results agree very well with the observations obtained by RHEED during the first stages of Nb growth in the growth regime I, that is, below 650 °C. In the beginning of deposition growth of epitaxial Nb(100) is observed, while after few atomic layers Nb growth continues in (110) orientation. The transformation thickness decreases with the growth temperature, see Section 2.3.

When the deposition rate is significantly increased, that is, by a factor of ten, Nb(100) is formed at 950 °C. At this growth rate,

the atoms are hindered to diffuse on the surface as there are successive atoms which bury them. Hence, the atoms stick to (100) growth which is according to Shim and Amar favorable for atom clusters and they cannot readjust to the energetically more favorable (110) configuration. On decreasing the growth rate (110) growth becomes possible again.

In general, we may state that the higher the energy of the deposited atoms and the higher the deposition rate (i.e., the higher the number of arriving atoms), the more probable is the stabilization of the (100) growth. This conclusion is consistent with the findings of Fu et al.<sup>[22]</sup> as well as other works where (100) growth is observed, such as Krishnan et al.<sup>[26]</sup> and Mattson et al.<sup>[27]</sup> Krishnan et al. use vacuum arc discharge with high energetic (>60 eV) Nb ions while Mattson et al. perform dc-magnetron sputtering

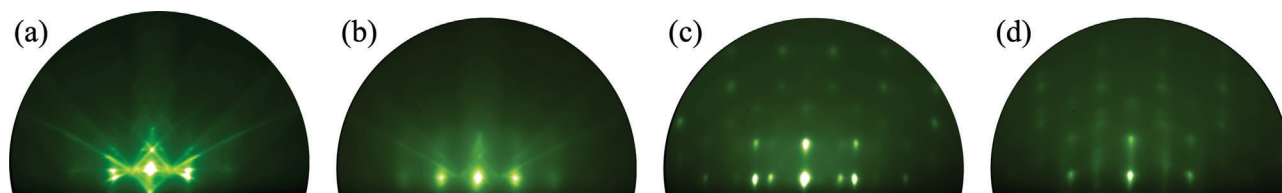


**Figure 7.** RHEED patterns of a) the MgO(001) single crystal, b) after growth of 0.4 nm Nb, and c) of 100 nm Nb at 500 °C. c) After cooling to RT, and d) after RT growth of 3 nm Pt. The images are taken with e-beam along the MgO[100] azimuth.

where the Nb ions also have higher kinetic energy than by utilizing thermal deposition.

The theoretical model of Shim and Amar in combination with the present results also explains the findings of Beringer et al.<sup>[20]</sup> They grew the Nb films by DC magnetron sputtering at 60 W and at 600 °C. Varying two parameters at the same time in two sample series they find either (110) and (100) orientation. The first parameter is the growth rate and was varied only slightly from 0.32 Å s<sup>-1</sup> to 0.48 Å s<sup>-1</sup>. In the present study the growth rate was increased to 4 Å s<sup>-1</sup> without any change of the crystalline orientation at the same growth temperature. This leads to the conclusion that the varied growth rate was not the deciding factor on the growth of different orientations. The second parameter varied by Beringer et al. is the surface quality. For the first series the MgO(100) substrates are annealed in situ at 600 °C, and (110) growth is observed, while for the second series a 2 nm MgO seed layer was deposited and Nb(100) was formed. Here, less oxygen vacancies are expected due to the fresh MgO(100) surface which then stabilizes Nb(100) growth. This is also consistent with our observation of a Nb(100) crystalline structure grown at room temperature on non-annealed MgO(100), which is expected to have a low oxygen vacancy concentration (results are not shown here).

In the present study all MgO(100) substrates were prepared by annealing in UHV which leads to the same (high) oxygen vacancy density throughout the MgO(100) surfaces. For this reason, the effect of surface quality which was observed by Beringer et al.<sup>[20]</sup> may be neglected here. Comparing the single phase Nb(110) thin films of region I (up to 600 °C) higher crystalline quality for higher growth temperature, with lower mosaicity, and increasing RRR is observed. As already pointed out by Beringer et al., the RRR is limited in this region by the inherently asymmetric biaxial morphology of grains. However, a spherical, more homogeneous surface morphology with (100) growth and with substantially higher RRR is achieved above 600 °C and/or with a seed MgO layer. In this region the Nb crystal lattice relaxes from (110) to (100) growth at about 4.5 nm. The proposed explanation for this mechanism is that after this thickness the effects of lattice mismatch and strain become less important than the in-plane diffusion of Nb species, which now have additional kinetic energy due to the increased temperature. Increasing the substrate temperature above 750 °C (region III), the thin Nb(110) layer is completely absent, and a fast diffusion of atoms is preponderant from the start. This though enables different scattering mechanisms, since the growth of larger and larger islands also creates irregular grain boundaries and defects, which hinder normal transport, as suggested by the upturn of the resistance at 10 K (Figure S5c, Supporting information) for samples grown above 750 °C. The same fractured surface morphology with (100) orientation and low RRR of 13.9, was obtained by using combined high Nb deposition rate and high growth temperature (Figure 2h). Similar argumentation applies to the low  $T_C$  observed for the sample grown at 950 °C. Even though the mosaicity is quite low, the facets observed in RHEED indicate the presence of a higher grain boundary density than which is seen in AFM (Figure 6d). These internal defects may act as energy barriers for conducting and superconducting electrons. The reason why the growth process at this temperature brings up again the (110) orientation is still under investigation. One explanatory model is an additional temper-

ature activated oxygen vacancy formation which becomes dominant over the fast Nb diffusion.

Another outcome of this study is the controlled tuning of the surface morphology. We have shown that the structure of the Pt cap layer is influenced by the Nb growth underneath. This can be important for the study of processes catalyzed by the Pt morphology, such as hydrogen absorption.<sup>[28]</sup>

## 4. Conclusion

The growth process of Nb on MgO(100) was studied in dependence of the growth temperature and the growth rate. The most thermodynamical stable growth orientation of Nb thin films on MgO(001) is the (110), but the formation of Nb(100) can be achieved under determined conditions, namely if the kinetic energy of Nb atoms is high enough, or if the oxygen vacancy density is low enough. The surface quality and preparation process of the substrate have to be considered first, as this will directly influence the nucleation of clusters. For the ideal MgO(100) surface the Nb(100) orientation is stabilized during growth, while for annealed MgO(100) an initial (100) nucleation of Nb can be expected, albeit followed by a rapid transition to the more stable (110). For annealed surfaces, the kinetic energy of the Nb atoms has to be taken into account. It can be tuned by choosing an appropriate deposition technique, ranging from the high energetic arc-discharge to the “soft” MBE deposition with low kinetic energy. In the latter case the (100) orientation may be stabilized by combining high growth temperature and high growth rate. Aside from the crystal orientation, the surface morphology is an essential factor to take into account when assessing the transport properties of these films. At least four different growth regions exist, associated with different grain shape and size, which are attainable with MBE growth at low enough growth rate. The findings help to understand preceding contradicting results and give a comprehensive view over the complex process of niobium growth on MgO(100).

## 5. Experimental Section

Niobium thin films were grown on MgO(100) substrates (Crystec GmbH) using a DCA M600 MBE system with a base pressure of  $5 \times 10^{-10}$  mbar. Before deposition, the substrates were cleaned from organic contaminations with ethanol and isopropanol ex situ and annealed at 600 °C in ultra high vacuum for 1 h. Nb was deposited by electron beam evaporation at typical growth rates of 0.4 Å s<sup>-1</sup> and 4 Å s<sup>-1</sup> at different substrate temperatures. For protection of the sample against oxidation a 3 nm Pt cap layer was grown at 0.4 Å s<sup>-1</sup> at room temperature on top of the Nb layer. The growth rates were calibrated by controlling the film thickness with X-ray reflectometry after deposition of about 10 nm Nb or Pt. Special care was taken with respect to the reproducibility of sample growth on varying the temperature. Hence, most of samples were fabricated at least twice. An example of the comparison of samples grown in the same conditions is shown in Figures S3 and S4, Supporting Information.

RHEED was measured in situ during deposition to trace the crystalline structure of the atomic layer being deposited. An electron beam of 15 keV energy was utilized. The surface morphology of the films was acquired by atomic force microscopy (AFM) using an Agilent technologies microscope operated in tapping mode.

X-ray diffraction (XRD) patterns were measured with a home-built diffractometer in Bragg Brentano geometry. The X-ray source was a copper anode, with a filter to select the Cu- $k_\alpha$  radiation. The scattered intensity was



collected at a DECTRIS 1D detector, which allows the mapping of a small portion of the reciprocal space and study the mosaicity of thin films. Additional XRD measurements were performed using a commercial Brucker D8 instrument, with copper anode and point detector.

The transport properties of the thin Nb layers were studied with a 4-probe technique.<sup>[29]</sup> An ac current with amplitude 100  $\mu$ A was applied in plane. The residual resistivity ratio was defined as  $R_{RR} = (295 \text{ K}) / (10 \text{ K})$ , and the superconducting transition temperature  $T_C$  was defined as the midpoint between the start and end of transition  $\Delta T_C$ . Raw transport data are shown in Figure S5a, Supporting Information.

## Supporting Information

Supporting Information is available from the Wiley Online Library or from the author.

## Acknowledgements

The authors would like to acknowledge the MLZ Physics Lab for the use of the D8 x-ray diffractometer, and in particular Alexander Book and Markos Skoulatos for their help and support.

## Conflict of Interest

The authors declare no conflict of interest.

## Data Availability Statement

The data that support the findings of this study are available from the corresponding author upon reasonable request.

## Keywords

epitaxy, MgO(100), Niobium, superconductivity, thin film growth, transport

Received: December 29, 2022

Revised: February 27, 2023

Published online:

- [1] R. Russo, *Meas. Sci. Technol.* **2007**, *18*, 2299.
- [2] A. A. Murthy, P. Masih Das, S. M. Ribet, C. Kopas, J. Lee, M. J. Reagor, L. Zhou, M. J. Kramer, M. C. Hersam, M. Checchin, A. Grassellino, R. d. Reis, V. P. Dravid, A. Romanenko, *ACS Nano* **2022**, *16*, 17257.
- [3] V. Bouchiat, M. Faucher, C. Thirion, W. Wernsdorfer, T. Fournier, B. Pannetier, *Appl. Phys. Lett.* **2001**, *79*, 123.

- [4] F. Arute, K. Arya, R. Babbush, D. Bacon, J. C. Bardin, R. Barends, R. Biswas, S. Boixo, F. G. Brandao, D. A. Buell, B. Burkett, Y. Chen, Z. Chen, B. Chiaro, R. Collins, W. Courtney, A. Dunsworth, E. Farhi, B. Foxen, A. Fowler, C. Gidney, M. Giustina, R. Graff, K. Guerin, S. Habegger, M. P. Harrigan, M. J. Hartmann, A. Ho, M. Hoffmann, T. Huang, et al. *Nature* **2019**, *574*, 505.
- [5] I. I. Soloviev, N. V. Klenov, S. V. Bakurskiy, M. Y. Kupriyanov, A. L. Gudkov, A. S. Sidorenko, *Beilstein J. Nanotechnol.* **2017**, *8*, 2689.
- [6] G. Wu, A.-M. Valente, H. Phillips, H. Wang, A. Wu, T. Renk, P. Provenzio, *Thin Solid Films* **2005**, *489*, 56.
- [7] G. Oya, M. Koishi, Y. Sawada, *J. Appl. Phys.* **1986**, *60*, 1440.
- [8] J. Lee, Z. Sung, A. A. Murthy, A. Grassellino, A. Romanenko, arXiv:2207.12495, **2022**.
- [9] E. Johansson, S. Olsson, C. Chacon, B. Hjörvarsson, *J. Phys.: Condens. Matter* **2004**, *16*, 1165.
- [10] A. Blomqvist, G. K. Pálsson, C. M. Araújo, R. Ahuja, B. Hjörvarsson, *Phys. Rev. Lett.* **2010**, *105*, 185901.
- [11] S. J. Callori, C. Rehm, G. L. Causer, M. Kostylev, F. Klose, *Metals* **2016**, *6*, 125.
- [12] S. Wagner, P. Klose, V. Burlaka, K. Nörthemann, M. Hamm, A. Pundt, *ChemPhysChem* **2019**, *20*, 1890.
- [13] L. Guasco, Y. N. Khaydukov, S. Pütter, L. Silvi, M. Paulin, T. Keller, B. Keimer, *Nat. Commun.* **2022**, *13*, 1486.
- [14] C. Majkrzak, J. Kwo, M. Hong, Y. Yafet, D. Gibbs, C. Chien, J. Bohr, *Adv. Phys.* **1991**, *40*, 99.
- [15] D. Devyaterikov, V. Vas'kovsky, V. Zhaketov, E. Kravtsov, M. Makarova, V. Proglyado, E. Stepanova, V. Ustinov, *Phys. Met. Metallogr.* **2020**, *121*, 1127.
- [16] I. Merino, L. Figueiredo, E. Passamani, V. Nascimento, F. Pelegrini, E. B. Saitovitch, *J. Magn. Magn. Mater.* **2017**, *432*, 494.
- [17] S. Di Nunzio, K. Theis-Bröhl, H. Zabel, *Thin Solid Films* **1996**, *279*, 180.
- [18] A. Wildes, J. Mayer, K. Theis-Bröhl, *Thin solid films* **2001**, *401*, 7.
- [19] T. E. Hutchinson, *J. Appl. Phys.* **1965**, *36*, 270.
- [20] D. B. Beringer, W. M. Roach, C. Clavero, C. E. Reece, R. A. Lukaszew, *J. Appl. Phys.* **2013**, *114*, 223502.
- [21] Y. Shim, J. G. Amar, *Surf. Sci.* **2016**, *645*, 80.
- [22] E. Fu, Y. Fang, M. Zhuo, S. Zheng, Z. Bi, Y. Wang, M. Tang, X. Ding, W. Han, H. Luo, J. Baldwin, A. Misra, M. Nastasi, *Acta Mater.* **2014**, *64*, 100.
- [23] X.-H. Pan, M. W. Ruckman, M. Strongin, *Phys. Rev. B* **1987**, *35*, 3734.
- [24] J. L. Du, Y. Fang, E. G. Fu, X. Ding, K. Y. Yu, Y. G. Wang, Y. Q. Wang, J. K. Baldwin, P. P. Wang, Q. Bai, *Sci. Rep.* **2016**, *6*, 33931.
- [25] A. Valente-Feliciano, H. Phillips, C. Reece, J. Spradlin, X. Zhao, D. Gu, H. Baumgart, D. Beringer, R. Lukaszew, B. Xiao, K. Seo, Proc. of 1st Int. Particle Accelerator Conf., IPAC'10, Old Dominion University, Norfolk, VA **2010**, pp.3055–3057.
- [26] M. Krishnan, E. Valderrama, B. Bures, K. Wilson-Elliott, X. Zhao, L. Phillips, A.-M. Valente-Feliciano, J. Spradlin, C. Reece, K. Seo, *Supercond. Sci. Technol.* **2011**, *24*, 115002.
- [27] J. E. Mattson, E. E. Fullerton, C. H. Sowers, S. D. Bader, *J. Vacuum Sci. Technol. A* **1995**, *13*, 276.
- [28] A. Chen, P. Holt-Hindle, *Chem. Rev.* **2010**, *110*, 3767.
- [29] Y. Khaydukov, S. Pütter, L. Guasco, G. Morari, R. Kim, T. Keller, A. Sidorenko, B. Keimer, *Beilstein J. Nanotechnol.* **2020**, *11*, 1254.